ACS Catalysis

Ruthenium (II) Complexes of CNC Pincers and Bipyridine in the Photocatalytic CO_2 Reduction Reaction to CO Using Visible Light: Catalysis, Kinetics, and Computational Insights

Leigh Anna Hunt,[⊥] Sanjit Das,[⊥] Robert W. Lamb,[⊥] Dinesh Nugegoda, Christine Curiac, Matthew T. Figgins, Ethan C. Lambert, Fengrui Qu, Nathan I. Hammer,[*] Jared H. Delcamp,[*] Charles Edwin Webster,[*] and Elizabeth T. Papish[*]

Cite This: *ACS Catal.* 2023, 13, 5986−5999

Read Online

ACCESS | Metrics & More | Article Recommendations | Supporting Information

Downloaded via MISSISSIPPI STATE UNIV on June 7, 2023 at 17:49:11 (UTC).
See https://pubs.acs.org/sharingguidelines for options on how to legitimately share published articles.

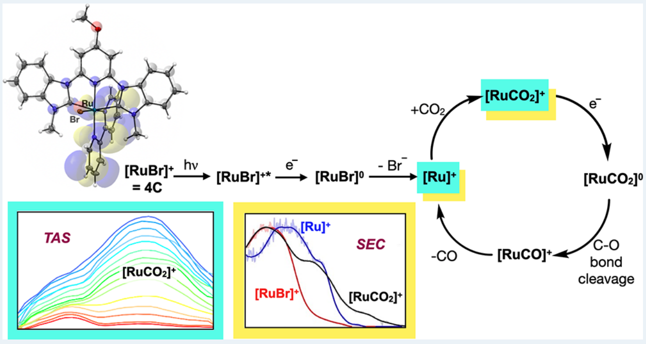

ABSTRACT: A series of five ruthenium (II) complexes containing a tridentate CNC pincer ligand, a bidentate 2,2′-bipyridine (bpy) ligand, and a monodentate ligand (chloride, bromide, or acetonitrile) were synthesized. The CNC pincer ligands used imidazole or benzimidazole-derived *N*-heterocyclic carbenes (NHCs) as the C donors and a 4-methoxy-substituted central pyridyl ring as the N donor. All of the complexes were characterized by analytical, spectroscopic, and single-crystal X-ray diffraction methods. These complexes were used as catalysts for visible-light-driven CO_2 reduction in the presence and absence of an external photosensitizer (PS). Notably, complex **4C** with a benzimidazole-derived CNC pincer ligand and bromide as the monodentate ligand was the most active catalyst tested for both sensitized and self-sensitized CO_2 reduction. Thus, this catalyst was the subject of further mechanistic studies using transient absorption spectroscopy (TAS), absorption spectroelectrochemistry (SEC), and computational studies. A mechanism has been proposed for self-sensitized CO_2 reduction involving (1) light excitation of the catalyst, (2) reduction by sacrificial donors, (3) halide loss, and (4) CO_2 binding to form $[\mathbf{RuCO_2}]^+$ as the catalyst resting state. The timeline for these steps and the structures of key intermediates are all supported by experimental observations (including TAS and SEC) and supporting computational studies. Subsequent steps in the cycle past $[\mathbf{RuCO_2}]^+$ were not experimentally observable, but they are supported by computations. Experiments were also used to explain the differences observed for sensitized catalysis. Catalyst **4C** is an unusually active catalyst for both sensitized and self-sensitized CO_2 reduction, and thus being able to understand how it functions and which steps are turnover-limiting is an important development facilitating the design of commercially viable catalysts for solar fuel formation.

KEYWORDS: *carbon dioxide reduction, photocatalysis, self-sensitized photocatalysis, transient absorption, spectroelectrochemical studies, pincer ligands, ruthenium*

■ INTRODUCTION

CO_2 is abundant, and it is a sustainable fuel precursor if used in carbon cycles with sunlight as the energy input. Artificial photosynthesis schemes using CO_2 as a raw material to generate fuels are therefore very attractive. However, CO_2 is stable and poorly reactive. In order to widely utilize CO_2 as a fuel, it must be reduced selectively and efficiently with sunlight as the energy input.[1−6] Selective reduction of CO_2 to CO is highly desired since CO can be used in the Fischer−Tropsch process to produce long-chain hydrocarbons as liquid fuels and complete the carbon fuel combustion cycle.[7] The use of molecular catalysts in the photocatalytic CO_2 reduction reaction (PCO_2RR) is attractive due to the relative ease of tunability with atomistic level control. However, a basic understanding of design principles for the introduction of rapid, selective, and robust molecular catalytic systems is needed.[8−20] To aid in rational design from first principles, systematic studies of structure−activity relationships and the observation of intermediate catalytic species in the PCO_2RR are critical. Photocatalysts allow for a unique opportunity to observe a single chromophore system, which is attractive for absorption spectroscopy-based studies that can be done under a variety of conditions, including both transiently and under steady-state

Received: November 6, 2022
Revised: April 4, 2023
Published: April 18, 2023

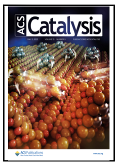

© 2023 American Chemical Society

https://doi.org/10.1021/acscatal.2c05459

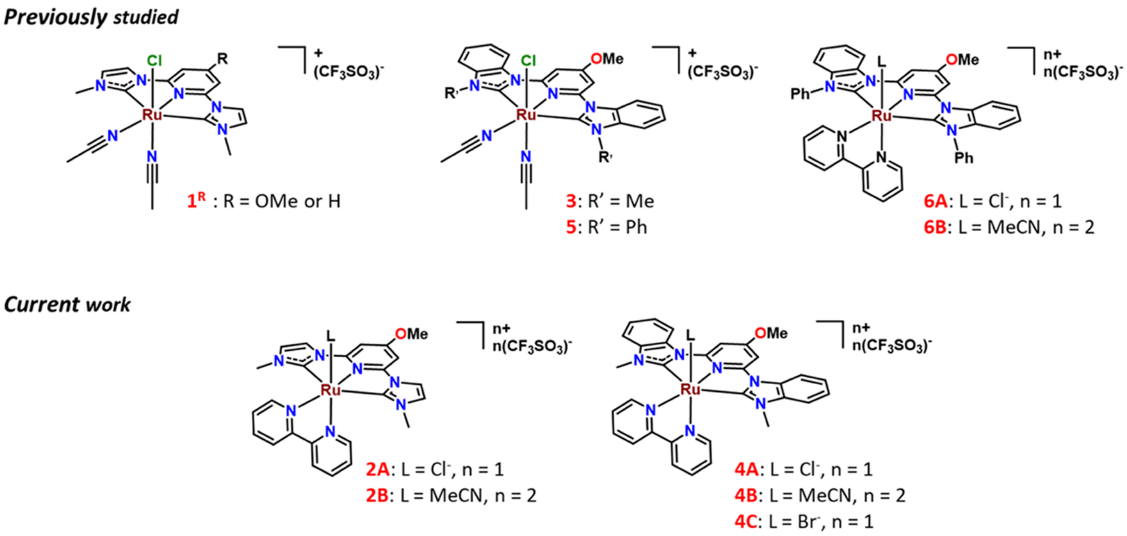

Previously studied

1^R : R = OMe or H

3: R′ = Me
5: R′ = Ph

6A: L = Cl⁻, n = 1
6B: L = MeCN, n = 2

Current work

2A: L = Cl⁻, n = 1
2B: L = MeCN, n = 2

4A: L = Cl⁻, n = 1
4B: L = MeCN, n = 2
4C: L = Br⁻, n = 1

Figure 1. Structures of the photocatalysts.

Scheme 1. Synthesis Routes Used to Form the Desired Complexes[a]

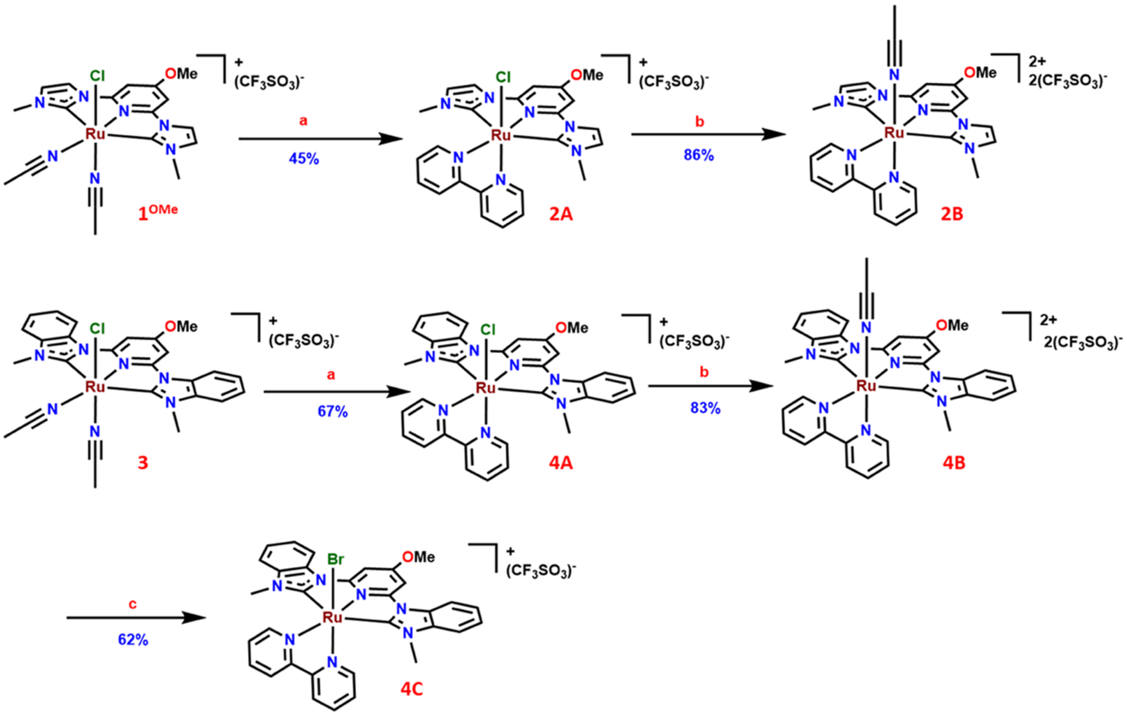

1^{OMe} 2A 2B 3 4A 4B 4C

[a] (a) 2,2′-bipyridine, methanol, 70 °C, 10−15 days; (b) CF_3SO_3Ag, acetonitrile, 80 °C, 16−20 h. (c) Et_4NBr, methanol, 50 °C, 15 days.

irradiation. Robust photocatalysts such as the record setting [Ru(CNC)(bpy)X]$^{n+}$ derived systems (Figure 1) provide an ideal entry point for such studies (bpy = 2,2′-bipyridine).[21]

NHCs and multidentate ligands containing NHCs are emerging as a powerful class of ligands in organometallics and homogeneous catalysis due to a strong σ donor ability, straightforward synthesis, and several possible modifications.[22−28] For example, NHC ligand donor strengths can be altered by saturation of the heterocycle, benzannulation, varying the *N*-substituents, or introducing a third heteroatom in the heterocyclic ring.[29−31] The combination of pyridine rings and NHCs have been used to make bidentate, tridentate, and tetradentate ligated metal complexes, which have found application in catalytic CO_2 reduction.[17,20,27,32−40] Unlike NHCs, pyridine is a weaker σ donor but can serve as a π acceptor, and substitutions on the pyridyl ring can provide another handle to further tune the electronics at the metal center. Tridentate CNC pincers consisting of a pyridyl ring and two NHC rings have often been used along with bipyridine in ruthenium chemistry (Figure 1).[33,41−43]

The addition of a bipyridine as a co-ligand with a CNC pincer ligated to the Ru center was found to be beneficial for self-sensitized (*i.e.*, no additional photosensitizer (PS) required) photocatalytic conversion of CO_2 to CO (*cf.*, **5** vs **6A** or **6B**; Figure 1).[21] The bpy co-ligand in **6B** shifts the LUMO from the CNC pincer in **5** to the bpy in the former, as shown computationally. Interestingly, **6B** was found to be a highly active photocatalyst for the self-sensitized reduction of CO_2 to

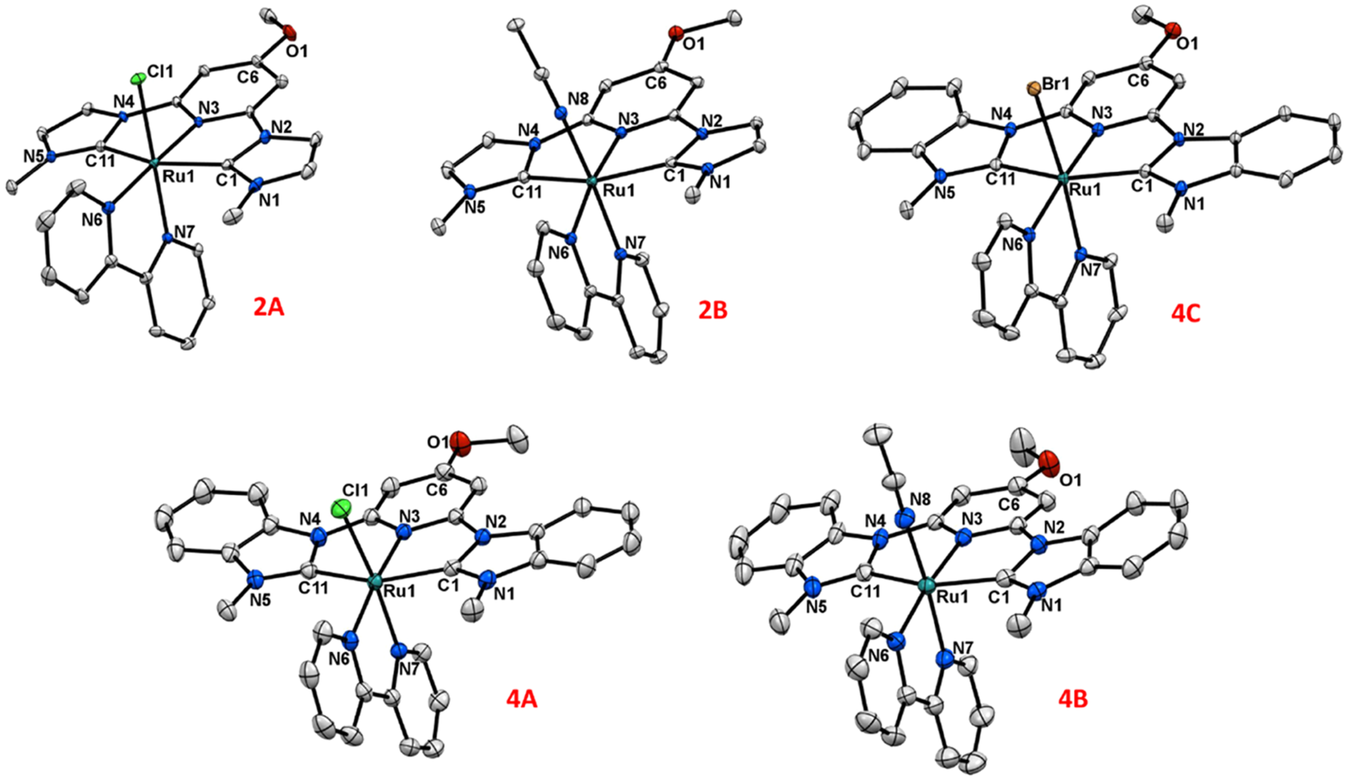

Figure 2. Molecular diagrams of complexes **2A**, **2B**, **4A**, **4B**, and **4C** based on crystallographic data with hydrogen atoms, solvent molecules (if any), and counteranions removed for clarity. Thermal ellipsoids are drawn at the 40% probability level.

CO.[21] Though visible light-driven and sensitized photocatalysis is well known for this reaction,[2,3,44] the self-sensitized CO_2 reduction is relatively rare because it requires one molecule to act as both catalyst and sensitizer.[12,17,18,45−50] Given the importance of a 4-methoxy pyridyl unit in the CNC pincer scaffold and a bpy co-ligand in our prior work, these groups are kept constant in this study with a focus on the role of different NHCs in photocatalysis.[39] Imidazole (**2A** and **2B**) and benzimidazole (**4A**, **4B**, and **4C**)-derived NHCs are known for differences in donor strength, with the former being a stronger donor.[29] Methyl wingtip groups for the NHC ligands were chosen for ease of synthesis as compared to the phenyl groups (in **6A** and **6B**). Furthermore, as shown herein, this change in wingtip substituents does not negatively impact catalyst performance. A monodentate ligand (L) is important for allowing a labile coordination site for substrate binding and catalysis. A labile neutral acetonitrile (**2B** and **4B**) is compared to the anionic chloride ligand (**2A** and **4A**). Finally, **4C** was considered for this study, as enhanced activity was recently reported for a Re-bromide catalyst as compared to its chloride analogue with the same ligand environment for the photocatalytic reduction of CO_2.[50] Herein, we experimentally investigate five novel Ru CNC pincer complexes (**2A**, **2B**, **4A**, **4B**, and **4C** in Figure 1) for their application in the photocatalytic reduction of CO_2 with a sacrificial electron donor (SED) system (SED system = 1,3-dimethyl-2-phenyl-2,3-dihydro-1*H*-benzo[*d*]imidazole (BIH) and triethylamine (TEA)) both in the presence and absence of an external PS ($Ir(ppy)_3$ where ppy = 2-phenylpyridine).

■ RESULTS AND DISCUSSION

Synthesis. The synthetic route to the target complexes is shown in Scheme 1. Syntheses of the CNC pincer ligand precursors and the corresponding $[(CNC)RuCl(MeCN)_2]^+$ complexes were previously described.[21,39] Complex $\mathbf{1}^{\mathbf{OMe}}$ undergoes a ligand substitution reaction with 2,2′-bipyridine in refluxing methanol for several days to form complex **2A** in 45% yield. This procedure is similar to our recently reported syntheses of related complexes.[34] Complex **2A** was then treated with silver triflate to replace the chloride with acetonitrile (from the solvent) to form complex **2B** in high yield (86%).[51] Complexes **4A** and **4B** were synthesized in a similar manner, in 67 and 83% yields, respectively, but starting from complex **3** bearing benzimidazole-derived NHCs.[51] The acetonitrile in **4B** was substituted with a bromide ligand to make the complex **4C** in 62% yield by treating **4B** with $^n Et_4NBr$ in methanol. In all of the complexes in this study, the coordination sphere of the ruthenium is completed by a tridentate CNC pincer, a bidentate bpy, and a monodentate halide (anionic) or acetonitrile (neutral) ligand. In solution at room temperature, these newly synthesized $[(CNC)RuL(bpy)]^{n+}$ complexes contain a mirror plane of symmetry, as is clear from the ^1H- and ^{13}C-NMR spectra.

Crystal Structures. The molecular diagrams of all of the ruthenium pincer complexes in this study (**2A**, **2B**, **4A**, **4B**, and **4C**) were determined by single-crystal X-ray diffraction (Figure 2). Our previously reported structures for $\mathbf{1}^{\mathbf{OMe}}$, **3**, **5**, **6A**, and **6B** have been used to compare the influence of different CNC pincer ligands on the bond lengths, bond angles, and the distortion of the pincer meridional CNC plane.[21,39] In all of the complexes used in this study, octahedral coordination of the ruthenium center is completed by a tridentate, a bidentate, and a monodentate ligand. All of the complexes are distorted from an ideal octahedral geometry with bond angles as low as ∼77° and as high as ∼103° (Table S3). The smaller angles are due to chelate ring constraints, and the larger angles typically involve atoms that are not chelated together (*e.g.*, in **2A**: N6-Ru1-C1 = 103.3(2)°).

The Ru−Cl bond distances decrease as the imidazole-derived NHCs are changed to benzimidazole-derived NHCs (Table 1).

Table 1. Ru−Cl Bond Distances (in Å)

	Ru−Cl		Ru−Cl
1^{OMe}	2.430(1)	**2A**	2.446(1)
3	2.417(5)	**4A**	2.431(1)
5	2.402(3)	**6A**	2.453(2)

A further decrease is noticed upon changing the *N*-wingtip substituents from methyls in **3** to phenyls in **5**. Substitution of two acetonitrile ligands in **1^{OMe}**, **3**, and **5** for a bpy ligand results in a slight increase in Ru−Cl bond lengths in **2A**, **4A**, and **6A**, respectively, as the bpy ligand has a stronger *trans* influence than the acetonitrile ligands. A similar *trans* influence and elongation of Ru−N bond lengths (relative to acetonitrile) are also observed in these complexes (Table S1). In general, the Ru−N6 (N6 is *trans* to the CNC pyridyl) bond length is always slightly elongated compared to Ru−N7 (N7 is *trans* to a halide or an acetonitrile) (Table S1). No additional notable differences in the bond distances involving the ruthenium center are noted (Table S1). The methoxy group on the pincer pyridyl ring serves as a π-donor with electron delocalization from the oxygen atom into the CNC pincer. Thus, the C6-O1 bond distance (average value = 1.347(1) Å) is in between typical C−O single and double bond lengths due to resonance (Table S2).

Electronic Spectra. The complexes were further characterized by UV−vis absorbance spectroscopy (Figure 3 (top), Table 2). The absorption spectra for the Ru complexes in this study show broad, multifeatured curves in the visible range with peaks between 400 and 500 nm with a shoulder extending to nearly 600 nm. The lowest energy transition for each of the complexes is assigned as a metal-to-ligand charge transfer (MLCT) event with the following trend observed for the wavelength of this band: **4B** < **2B** < **4C** ≅ **4A** < **2A**. This trend shows that in all cases, the MeCN-ligated complexes absorb light of higher energy than the halide bound complexes with minimal difference between the Cl and Br ligated complexes. Because the lowest energy MLCT event is predicted to be a Ru-to-bpy electron transfer primarily, the MeCN ligands are expected to blue-shift the absorbance spectrum relative to halides due to the MeCN groups participating in π-back bonding and reducing the electron density at the Ru center. Similarly, the benzimidazole-derived CNC ligands also blue-shift the lowest energy absorbance features relative to imidazole-derived CNC ligands, likely again due to the increased π-back bonding for the benzimidazole-derived ligand. Density functional theory (DFT) and time-dependent (TD) DFT were carried out to analyze the nature of the lowest energy transition at the SMD-PBE0-D3BJ/BS1 level of theory. The hole to particle transition (highest occupied transition orbital, HOTO, to lowest unoccupied transition orbital, LUTO) were observed to have significant oscillator strengths via TD-DFT, which suggests these transitions are visible experimentally. The observed MLCT bands involve an electronic transition from a ruthenium-centered HOMO (or hole) to a bpy ligand-based LUMO (or particle), as shown in Figures 4 and S43.

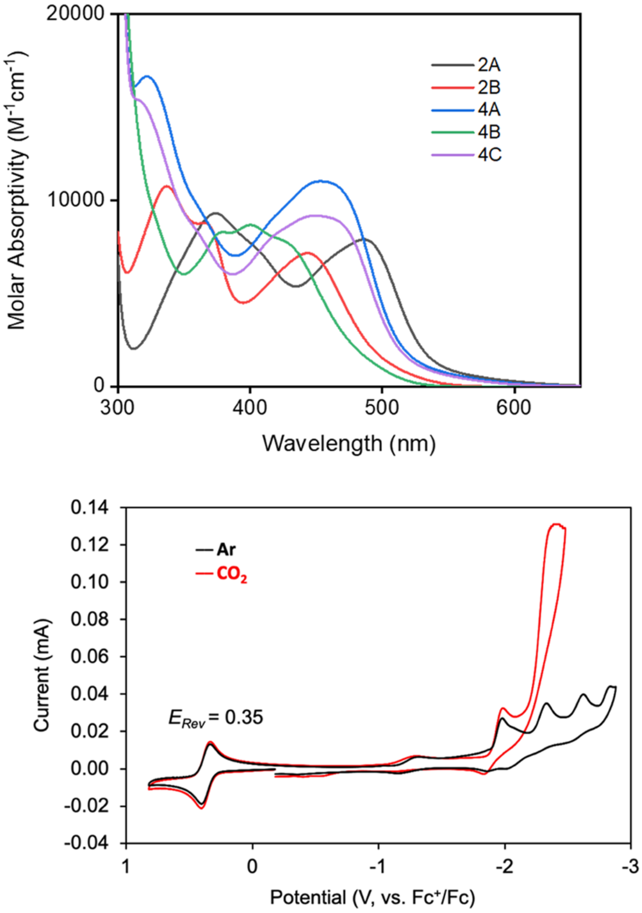

Figure 3. Absorbance spectra of Ru complexes in MeCN (top) and a representative CV of **4C** within the experimental window (bottom).

Electrochemical Studies. Electrochemical studies were undertaken *via* cyclic voltammetry (CV) both under Ar and CO_2 atmospheres (Table 2 and Figures 3 (bottom) and S31). This allowed us to probe the ability of these complexes to reduce CO_2 electrochemically and their thermodynamic compatibility with the PS under photocatalytic conditions. Both under Ar and CO_2, all complexes showed one oxidation and multiple reduction events within the experimental window. The oxidation event was generally reversible and appeared to be metal-centered (Ru(II) to Ru(III)). The complexes with benzimidazole-derived CNC ligands were oxidized at more positive potentials compared to their imidazole analogues with the same monodentate ligands (*cf.* **4A** (0.32 V) vs **2A** (0.19 V) and **4B** (0.78 V) vs **2B** (0.64 V)). Also, the complexes with acetonitrile ligands were oxidized at higher potentials compared to the more electron-rich complexes with a halide. Among these complexes, **2A** was oxidized at the least positive potential and it absorbed (UV−vis absorption) at the longest wavelength for the lowest energy transition. Other reduction events also followed similar trends, with Ru complexes of benzimidazole-derived CNC ligands being reduced at less negative potentials compared to their imidazole analogues when comparing systems with the same monodentate ligands. Under the CO_2 atmosphere, moderate current enhancement was observed with these complexes supporting electrocatalytic CO_2 reduction beyond the first reduction event. However, the reduction products were not identified, but based upon the photochemical studies below, CO formation is likely. Complex **2B** was found to be the best electrocatalyst and moderately active, with the following order of reactivity **2B** > **4B** > **2A** > **4C** > **4A** from i_{cat}/i_p values. It can be noted that the acetonitrile complexes were better electro-

Table 2. Electronic Spectral Features and Cyclic Voltammetry Studies (under Ar and CO_2) of the Ru Complexes Reported Herein in MeCN[a]

	λ_{max} (nm)	ε (M^{-1} cm^{-1})	$E_{(S/S-)}{}^{peak\ Ar}$	$E_{(S-/S2-)}{}^{peak\ Ar}$	$E_{(S-/S2-)}{}^{peak\ CO2}$	$E_{(S-/S2-)}{}^{onset\ CO2}$	i_{cat}/i_p	$E_{Rev\ Ru(II)/Ru(III)}$
2A	486	7900	−2.07	−2.46	−2.81	−2.27	4.0	0.19
2B	444	7200	−1.95	−2.46[b]	−2.52	−2.09	5.2	0.64
4A	454	11,100	−2.02	−2.35	−2.36	−2.12	3.2	0.32
4B	400	8600	−1.90	−2.32[b]	−2.44	−2.07	4.4	0.78
4C	449	9200	−1.98	−2.33	−2.40	−2.12	3.7	0.35

[a] Reduction potentials are given in V against Fc^+/Fc. [b] Third reduction wave values are reported.

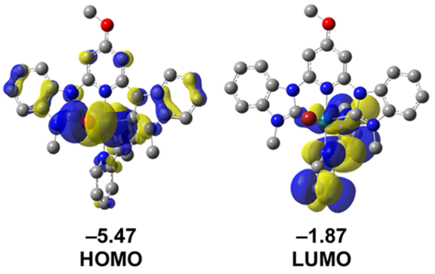

Figure 4. HOMO and LUMO orbitals of **4C**. See Figure S38 for orbital images of **2A**, **2B**, **4A**, and **4B**.

catalysts compared to the halo-complexes. In general, complexes with imidazole-derived CNC were found to be slightly better electrocatalysts compared to their benzimidazole analogues.

Photocatalysis. Photocatalytic experiments were carried out under white light LED irradiation with the light intensity set to match that of the solar spectrum in power (~64 mW/cm^2) for photons between 400 and 700 nm. Each catalyst was evaluated both with and without $Ir(ppy)_3$ added as a photosensitizer (PS) since all of the complexes absorb in the visible spectral region. $Ir(ppy)_3$ is a commonly used PS with a reduction potential negative enough for a favorable free energy for electron transfer from the reduced PS to the Ru complexes to take place (Figure S31 and Table 2). 1,3-Dimethyl-2-phenyl-2,3-dihydro-1*H*-benzo[*d*]imidazole (BIH) was used as a strong sacrificial electron donor (SED) with added triethylamine (TEA) to deprotonate BIH after electron transfer to give irreversible electron transfers. Photocatalysis reactions in this study were carried out in anhydrous acetonitrile (2 mL) with 1×10^{-6} M catalyst, 1×10^{-4} M of $Ir(ppy)_3$, 0.01 M of BIH, and 0.36 M of TEA under CO_2 atmosphere. In the photocatalytic reactions, only CO is observed in the reactions discussed below, with no appreciable H_2, CH_4, CH_3OH, or HCO_2^- observed by GC or ^1H NMR.

The turnover number (TON: number of moles of CO/number of moles of catalyst) order observed is: **4C** ≫ **2B** > **2A** ≫ **4A** > **4B** under PS free conditions (Figure 5, Table 3). The bromide-ligated **4C** complex shows substantially higher durability than the other catalysts. In terms of turnover frequency (TOF), only **4C** shows no significant activation period, with the earliest calculated TOF being the same as the maximum observed TOF value (Figure 6, Table 3). The remaining complexes show an initial slow period prior to reaching a maximum TOF (TOF_{max}) at ≥24 h. Notably, the TOF_{max} trend follows the same trend as observed for the TON values. The origin of the initial slow TOF period observed for all of the catalysts except **4C** is not obvious from these studies. TON and TOF trends do not track with CNC ligand selection or with MeCN versus halide selection. This suggests that an induction period of unknown origin is required for these precatalysts (**2A**, **2B**, **4A**, and **4B**) in the photocatalytic CO_2 reduction reaction.

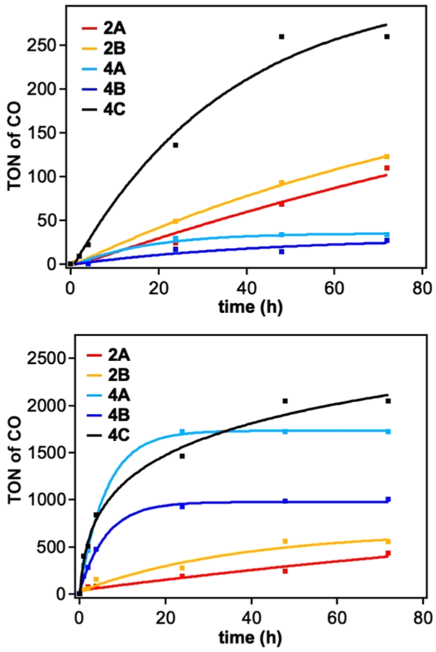

Figure 5. Turnover number versus time plots without added PS (top) and with added PS (bottom).

Table 3. Catalytic Parameters with and without Added PS

cat.	time (h)[a]	TON (CO)	TOF_{init} (h^{-1})[b]	TOF_{max} (h^{-1})[c]
		Without Added $Ir(ppy)_3$		
2A	72	110	0.5	1.8 @ 48 h
2B	72	122	0.8	2.2 @ 24 h
4A	48	33	0.1	1.4 @ 24 h
4B	72	27	0.0	0.8 @ 24 h
4C	48	260	6.5	6.5 @ 4 h
		With Added $Ir(ppy)_3$		
2A	72	430	47	47
2B	48	558	45	51
4A	24	1720	298	298
4B	72	1002	186	186
4C	48	2046	395	395

[a] Indicates when the reaction stopped producing CO or 72 h was reached. [b] Initial TOF values are reported at 4 h in the absence of $Ir(ppy)_3$ to improve accuracy when low amounts of product is forming. Values are reported at 1 h in the presence of $Ir(ppy)_3$. [c] TOF_{max} values are all reported at 1 h in the presence of $Ir(ppy)_3$.

When the PS is added to the reaction mixture, a new TON and TOF trend is observed as follows: **4C** > **4A** > **4B** > **2B** > **2A**. Interestingly, all of the benzimidazole-based CNC-derived complexes are significantly higher in TON and TOF than the

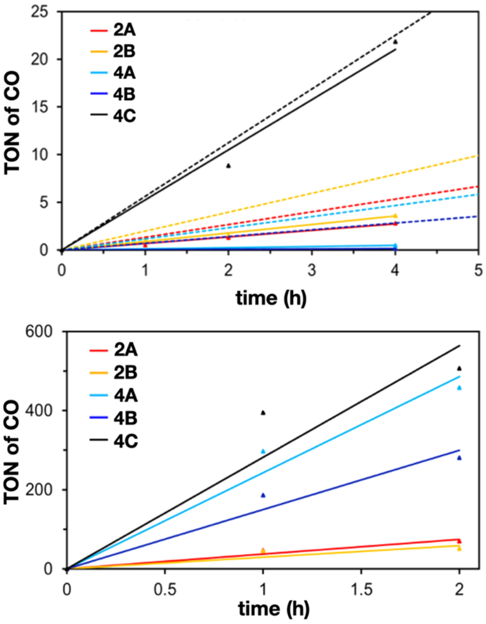

Figure 6. TON measurements without added PS (top) and with added PS (bottom) at early time points. The slope of the solid lines shows the TOF_{init} values for each catalyst. The slope of the dashed lines shows the TOF_{max} rate on the graph (top) without added photosensitizer. The discrepancy between TOF_{max} and TOF_{init} is apparent from the distance between the dotted and solid lines for **2A**, **2B**, **4A**, and **4B**.

imidazole-based CNC-derived catalysts by about ≥2 times irrespective of the monodentate ligand. For the benzimidazole-derived catalysts, faster and more durable catalysis was observed when the monodentate ligand was a halide rather than an acetonitrile. This is somewhat surprising because MeCN ligands are often considered more labile (cf. halide), and MeCN is present in solvent quantities. Typical catalytic mechanisms proposed in the literature suggest halide dissociation should occur as an initial step to give the same active catalyst from either the halide or MeCN complexes. This suggests that dissociation of MeCN from a reduced complex may be slow.[37] When the PS is present, the initial TOF (at 1 h) and TOF_{max} rates are effectively the same, with no evidence of a slow catalysis induction period. The TON and TOF values are also higher when a PS is present with an up to 52 times increase in TON (with **2A**) and an up to 230 times increase in TOF (with **4B**).

However, we note that examples of photocatalysts (no added PS) in the literature are rare.[12,17,18,45−50] There are potential advantages to these systems in photoelectrochemical cells (PECs). All-in-one photocatalysts have fewer electron transfer steps to circumvent any sluggish kinetics for electron transfer reactions from the PS to the semiconductor or from the reduced PS to the catalyst. The elimination of an unnecessary electron transfer reaction results in a theoretically more efficient system with fewer thermal losses. Despite the lower performances of photocatalysis systems in the absence of a PS, these systems remain attractive for further study. Under both sets of conditions (with and without PS), **4C** remains the most active catalyst among the complexes studied. Thus, this complex was selected for more in-depth studies via time-resolved spectroscopy.

Spectroelectrochemical Studies. Spectroelectrochemical (SEC) absorption studies were undertaken with **4C** under Ar (Figure 7). To facilitate the discussion, complex **4C** can be abbreviated as $[\mathbf{RuBr}]^+$, where the brackets "[ ]" refer to the CNC and bpy ligands, which are always present as **4C** undergoes transformations. Under Ar, the absorption of $[\mathbf{RuBr}]^+$ red-shifts in onset value by ~75 nm under reducing conditions to give a new species assigned as $[\mathbf{Ru}]^+$, which has a shoulder present at 550 nm. Computationally, this spectral shift is also observed via TD-DFT computations, where the lowest energy vertical transition of **4C** or $[\mathbf{RuBr}]^+$ is at 416 nm, and the lowest energy vertical transition of $[\mathbf{Ru}]^+$ (which is the product of bromide loss after reduction) with a strong oscillator strength is located at 528

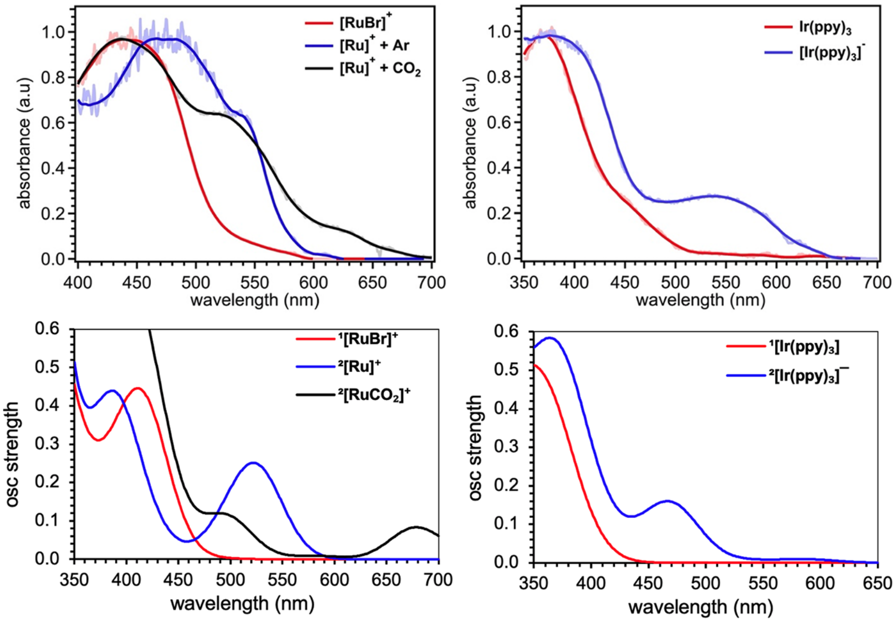

Figure 7. Top: SEC data with **4C** = $[\mathbf{RuBr}]^+$ (at −1.8 V versus NHE) and $Ir(ppy)_3$ (at approximately −2.8 to −3.0 V versus NHE) in MeCN in the presence of 0.1 M n-Bu_4NPF_6 with a platinum working honeycomb electrode, platinum counter electrode, and an Ag/AgCl reference electrode. The SEC spectra have substantial noise below 400 nm experimentally. Bottom: Simulated absorbance spectra of $^1[\mathbf{RuBr}]^+$, $^2[\mathbf{Ru}]^+$, and $^2[\mathbf{RuCO_2}]^+$ (left) and $^1[\mathbf{Ir(ppy)_3}]$ and $^2[\mathbf{Ir(ppy)_3}]^-$ (right). For $^2[\mathbf{RuCO_2}]^+$, the oscillator strength for has been scaled by 5.

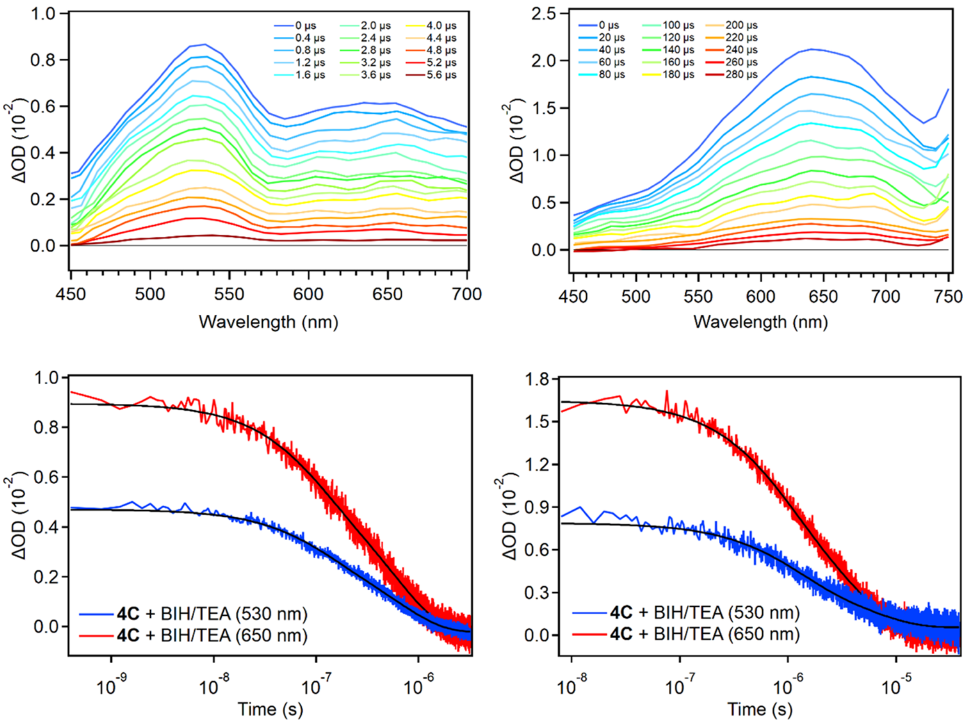

Figure 8. Transient absorption spectroscopic studies of **4C** (λ_{exc} = 355 nm, <10 mJ/pulse). Top left: Transient absorption spectrum of photoexcited **4C** in N_2-saturated MeCN with BIH/TEA. Top right: Transient absorption spectra of photoexcited **4C** in CO_2-saturated MeCN with BIH/TEA. Bottom left: Single wavelength absorption changes of **4C** at 530 nm (blue) and 650 nm (red) under N_2. Bottom right: Single wavelength absorption changes of **4C** at 530 nm (blue) and 650 nm (red) under CO_2.

Table 4. Lifetimes Obtained from Fitting of Single Wavelength Absorption Changes (λ_{exc} = 355 nm, <10 mJ/pulse)

sample	$\tau_{530nm,N2}$ (μs)	$\tau_{530nm,CO2}$ (μs)	$\tau_{650nm,N2}$ (μs)	$\tau_{650nm,CO2}$ (μs)
4C/BIH/TEA	6.0	325	7.0	300
Ir(ppy)$_3$/BIH/TEA			2700	
Ir(ppy)$_3$/**4C**/BIH/TEA	1900	2100	140/1700	180/1700

nm (Figure 7 (bottom left) and Figures S43 and S45). These trends are in line with data for the prototypical [Ru(bpy)$_3$]$^{2+}$ ion. Upon reduction, the main absorption band of [Ru(bpy)$_3$]$^{2+}$ undergoes a red shift.[52] Our computational methodology nicely reproduces these trends in both [Ru(bpy)$_3$]$^{2+}$ (Figure S48) and **4C**, lending credence to the assignments of the new absorption features as the reduced species.

To electrochemically simulate the absorption signal of CO_2 bound to **4C**, absorption SEC was also done under a CO_2 atmosphere in a CO_2-filled box. A new absorption signal with an absorption maximum at 440 nm and shoulders at 530, 630, and 670 nm arises when [**RuBr**]$^+$ is reduced under CO_2 in the absence of protons. New absorption bands are distinctly blue-shifted (550−530 nm) and red-shifted (610−630 and 670 nm) from the absorption band arising in the SEC of reduced **4C** under Ar, suggesting the formation of a new species. Notably, the band at 530 nm may only appear to shift as the overlapping band at 500 nm with [**RuBr**]$^+$ changes to 440 nm upon reduction. This new species can tentatively be presumed to be a Ru−C bonded species with the carbon arising from CO_2 such as with [**RuCO$_2$**]$^+$ or [**RuCO**]$^+$ if a disproportionation reaction ($2CO_2 + 2e^-$ -> $CO + CO_3^{2-}$) is occurring in the absence of protons, as suggested by the CV data showing current increases under dry conditions (see below for the proposed structures related to these species). The combined evidence, including that Figures 7 (bottom left) and S46 show a peak at 678 nm, favors assigning this new species as [**RuCO$_2$**]$^+$.

Similarly, the absorption SEC spectrum of Ir(ppy)$_3$ reveals a red-shifted anion with the shoulder of Ir(ppy)$_3$ at 450 nm shifting to 545 nm upon reduction at −2.8 V. These results are again consistent with the TD-DFT results obtained for Ir(ppy)$_3$ and [Ir(ppy)$_3$]$^-$, which suggest a red shifting of the reduced PS (Figures 7 (bottom right) and S37). The SEC results under Ar reveal that a valuable spectral signature is available for **4C** upon reduction, which can be monitored via transient absorption spectroscopy (TAS). However, if Ir(ppy)$_3$ is present, then overlapping signals for reduced species would be present in the TAS results (Figures 7 and S37).

Transient Absorption Spectroscopy. Nanosecond transient absorption spectroscopy (TAS) was used to obtain information regarding the photocatalytic behavior of **4C** under varied environments. Photoexcitation of an N_2-saturated MeCN solution of **4C** and BIH/TEA induced a broad transient absorption spectrum in the visible region with an absorption maximum at 530 nm and featureless absorption that extends past 700 nm (Figure 8). The appearance of a band near 530−550 nm is consistent with SEC data obtained under an inert atmosphere. The observed absorption features formed within the duration of the excitation pulse and decayed with no variation in spectral shape.

Single wavelength absorption changes monitored at 530 and 650 nm were adequately described by a single exponential function with corresponding lifetimes of 6.0 and 7.0 μs, respectively (Table 4). Notably, SEC shows new features at 550 nm and weakly at 610 nm, which are at similar wavelengths to the TAS signals. It is possible that the species observed near 530 nm is the result of an electron transfer reaction to form $[\mathbf{RuBr}]^0$ transiently followed by a chemical reaction (an EC mechanism) such as loss of a bromide ligand to form $[\mathbf{Ru}]^+$, which is thought to be thermodynamically favorable based on prior studies. Thus, the peak at 530 nm is assigned to $[\mathbf{Ru}]^+$, though some equilibrium with the acetonitrile bound complex, $[\mathbf{RuNCCH_3}]^+$, cannot be ruled out. In the simulated spectrum for the bromide loss product, $[\mathbf{Ru}]^+$, there is an electronic transition at 528 nm (see Figure 7 (bottom left) and Figure S45), which is primarily *d* to *d* in nature, with the excited configuration exhibiting a prominent feature in the open coordination site.

The transient absorption spectrum observed after photoexcitation of a CO_2-saturated MeCN solution of **4C** with BIH/TEA presented an absorption maximum at 650 nm, which is at a similar wavelength to the signal observed at 670 nm in the SEC experiment under CO_2. The feature at 650 nm formed within the duration of the excitation pulse and decayed with an estimated lifetime of ∼300 μs. The TAS data is also consistent with the SEC data showing a single new feature at 530 nm, which corresponds to the longer-lived signal via TAS. Based on this analysis, the signal at 530 nm is assigned as $[\mathbf{Ru}]^+$, the bromide loss product (*vide infra*). The signal present at 650 nm via TAS corresponds to the CO_2 binding product, $[\mathbf{RuCO_2}]^+$, which has a predicted absorbance at 678 nm (Figures 7 and S46). Interestingly, the decay rates of the species formed under CO_2 are significantly slower than under N_2. Although the reason for this change in rates is not apparent, it may be related to the experiment, with CO_2 having all of the necessary components to undergo a full catalytic cycle, which could lead to the generation of a single species if a slow step is present in the catalytic cycle or due to one of the species having a different identity under N_2 vs CO_2 (*vide infra*).

Given the reductive pathway of $Ir(ppy)_3$ present in the reaction solution, transient absorption measurements were also carried out for $Ir(ppy)_3$ with the SD system. The transient absorption spectrum of an N_2-saturated MeCN solution of $Ir(ppy)_3$ and BIH/TEA exhibited two positive absorption bands at 370 and 650 nm (Figure 9). Single wavelength absorption changes monitored at 480 and 650 nm were described by a single exponential function with corresponding lifetimes of 2.8 and 2.7 ms, respectively (Table 4; Figure S33).

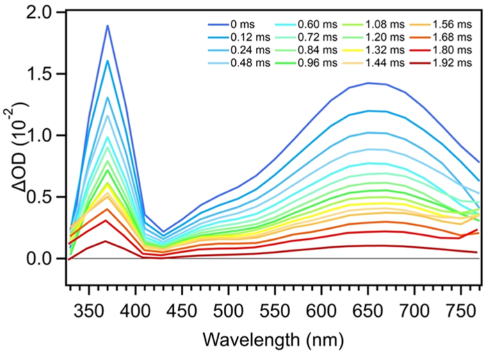

Figure 9. Transient absorption spectra of $Ir(ppy)_3$ with BIH/TEA following 355 nm laser excitation in N_2-saturated MeCN.

When **4C** is added to the reaction solution (with $Ir(ppy)_3$ and BIH/TEA present) under N_2, the excited-state dynamics differ significantly from those observed without $Ir(ppy)_3$. A broad transient absorption spectrum is observed with an absorption maximum at 650 nm, which resembles that of $[Ir(ppy)_3]^-$ on short timescales (Figure 9). After rapid decay of the 650 nm absorption feature (representing $[Ir(ppy)_3]^-$), the transient absorption resembles that of $[\mathbf{Ru}]^+$, with a diagnostic peak at 530 nm and broad absorption that extends past 700 nm. The absorption features at 530 and 650 nm overlap significantly in the visible region, which convolutes the time-dependent absorption changes monitored at each absorption maximum. The signals at 530 and 650 nm decay with estimated lifetimes of 1.9 and 1.7 ms, respectively.

The absorption band at 530 nm (Figure 10) is attributed to a combination of $[Ir(ppy)_3]^-$ and $[\mathbf{Ru}]^+$, which absorb in this range (Figures 7 and S45). This renders the kinetics at 530 nm difficult to interpret; however, we note that under catalytic conditions, the $Ir(ppy)_3$ PS is present in 100-fold excess, which may mean the signals observed are predominately due to the presence of $Ir(ppy)_3$-related signals. Under N_2, a strong signal at ∼530 nm is observed, which is assigned to $[Ir(ppy)_3]^-$, given the higher concentration of $Ir(ppy)_3$ and the presence of $[Ir(ppy)_3]^-$ at this wavelength, as observed via SEC (Figures 7 and 10). The decay rate of the 530 nm signal with added $Ir(ppy)_3$ is dramatically slower than the rate observed for $[\mathbf{Ru}]^+$ without $Ir(ppy)_3$ under N_2, which further suggests this signal is due to an $Ir(ppy)_3$-related signal (Table 4: 1.9 ms versus 6.0 μs).

When N_2 was replaced with CO_2, the transient absorption spectrum again resembled that of $[Ir(ppy)_3]^-$ at early time delays with an absorption maximum at 650 nm. However, the decay of 650 nm into the 530 nm baseline is considerably slower when CO_2 is present in the reaction solution. The transient absorption feature centered at 530 nm is attributed to a combination of $[Ir(ppy)_3]^-$ and $[\mathbf{Ru}]^+$ species and decays with an estimated lifetime of 2.1 ms (Figure 10). The 650 nm signal decays biexponentially with estimated lifetime components of 180 μs and 1.7 ms, respectively. A bromide ligand dissociation from $[\mathbf{RuBr}]^0$ (formed transiently by reduction of $[\mathbf{RuBr}]^+$) slowing significantly in the presence of $Ir(ppy)_3$ seems unlikely; thus, this signal at 650 nm is not ascribed to $[\mathbf{RuBr}]^0$. However, the signal at 650 nm has a lifetime that is more than five times as long in the presence of $Ir(ppy)_3$ (300 μs versus 1700 μs). Thus, the species formed at 650 nm under CO_2 can be assigned to the product of CO_2 addition to $[\mathbf{Ru}]^+$, namely, $[\mathbf{RuCO_2}]^+$. This is substantiated by the dramatically large increase in lifetime (∼40× increase) observed under CO_2 when compared to under N_2 with no $Ir(ppy)_3$ present. Interestingly, upon addition of $Ir(ppy)_3$, the signal at 650 nm under CO_2 has a significantly shortened lifetime (300 versus 180 μs for the fast component). This would be consistent with the $[Ir(ppy)_3]^-$ species undergoing an electron transfer reaction with the $[\mathbf{RuCO_2}]^+$ adduct leading to more rapid consumption and thus increased production of $[\mathbf{RuCO_2}]$. These species are incorporated into the catalytic cycle described in the next section.

Mechanistic Discussion. Having found several intermediates observable by TAS, emission spectroscopy, and SEC measurements, the steps of a catalytic cycle were analyzed by DFT to evaluate steps in the mechanism for favorable thermodynamics and agreement with the experimental data (Figures 11 and 12). All computations were performed using the

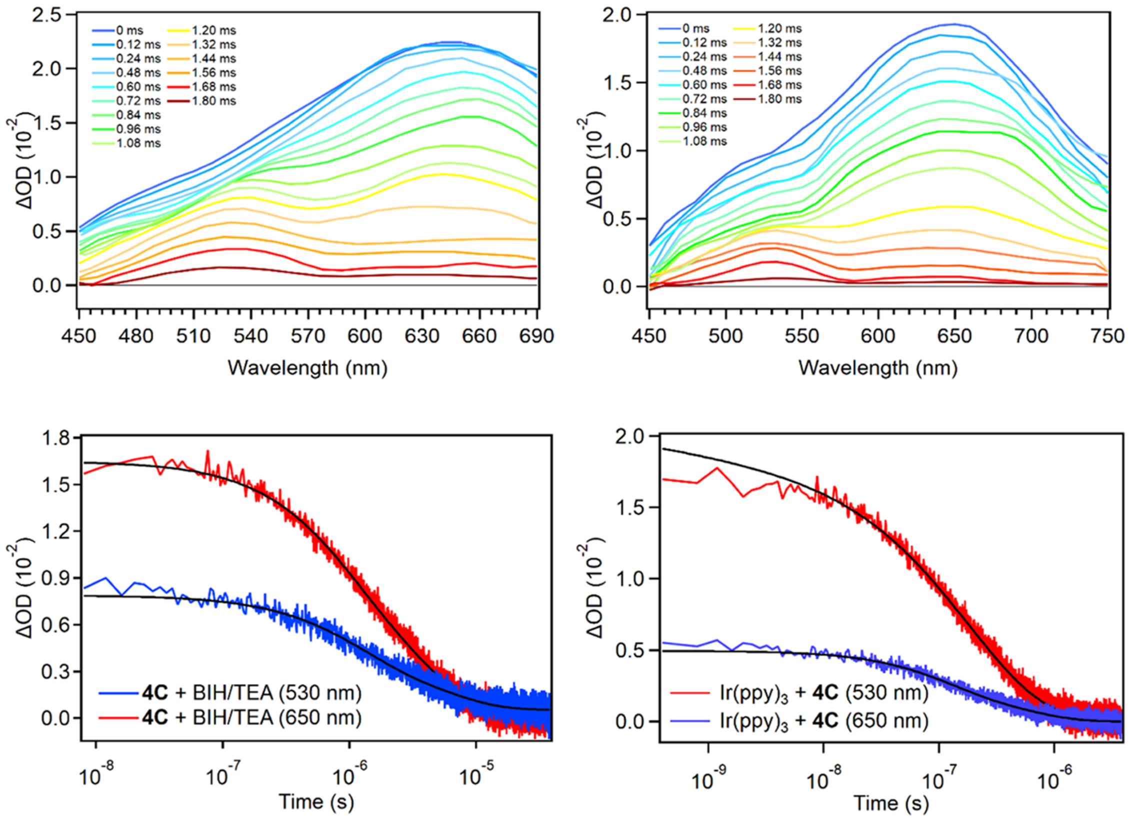

Figure 10. Transient absorption spectra of **4C** with Ir(ppy)$_3$ and BIH/TEA following 355 nm laser excitation in N$_2$ (top left) or CO$_2$ (top right)-saturated MeCN. Bottom left: single wavelength absorption changes of Ir(ppy)$_3$ and **4C** with BIH/TEA at 530 nm (blue) and 650 nm (red) under N$_2$. Bottom right: single wavelength absorption changes of Ir(ppy)$_3$ and **4C** with BIH/TEA at 530 nm (blue) and 650 nm (red) under CO$_2$.

PBE0 functional with GD3BJ empirical dispersion. The basis sets used were mod-LANL2DZ for the heavy atoms and 6−31G(d′) for all other atoms. An implicit SMD solvation model equivalent to acetonitrile for the solvent was also employed for all computations (full details are in the Computational Methods section). For the nonphotosensitized system (only **4C** = [**RuBr**]$^+$; no Ir(ppy)$_3$), the following equations were analyzed.

$$[\mathbf{RuBr}]^{+} + h\nu \rightarrow [\mathbf{RuBr}]^{+*} \tag{1}$$

$$[\mathbf{RuBr}]^{+*} + \mathrm{BIH} \rightarrow [\mathbf{RuBr}]^{0} + \mathrm{BIH}^{+} \tag{2}$$

$$[\mathbf{RuBr}]^{0} \rightarrow [\mathbf{Ru}]^{+} + \mathrm{Br}^{-} \tag{3}$$

$$[\mathbf{Ru}]^{+} + \mathrm{CO_2} \rightarrow [\mathbf{RuCO_2}]^{+} \tag{4}$$

Equation 1 is observed by absorption spectroscopy, and prolonged irradiation of **4C** in the absence of BIH/TEA shows no change in the catalyst structure by NMR (Figure S34). Thus, eq 1 occurs without breaking of the chemical bonds within the catalyst. Subsequently, [**RuBr**]$^{+*}$ is quenched with BIH to give [**RuBr**]^0 (Figures 11 and 12). Equation 2 is computed to be exergonic whether it occurs from a triplet (^{3}[**RuBr**]$^{+*}$ with $\Delta G = -9.3$ kcal/mol) or singlet (^{1}[**RuBr**]$^{+*}$ with $\Delta G = -12.3$ kcal/mol) excited state.

The singly reduced [**RuBr**]^0 can generate [**Ru**]$^+$ (eq 3), which is observed at ~530 nm by SEC and TAS. This bromide dissociation is predicted to be uphill ($\Delta G = 5.8$ kcal/mol) from the singlet excited state, but the process is exergonic ($\Delta G = -3.4$ kcal/mol) from the triplet excited state (reduction of ^{3}[**RuBr**]$^{+*}$, then dissociation of a bromide). We cannot rule out the participation of solvent in this step via CH$_3$CN binding to [**Ru**]$^+$, which could be the broad signal observed at ~650 nm using SEC or TAS under an inert atmosphere. The binding of CO$_2$ to [**Ru**]$^+$ to form [**RuCO$_2$**]$^+$ is observed at 650 nm via TAS and SEC, and the ΔG is predicted to be 7.3 kcal/mol uphill in energy (eq 4). While both steps (eqs 3 and 4) are uphill in energy from the singlet states, neither step is prohibitively high in energy, and thus they should be viable at room temperature in solution.

The remaining steps of the catalytic cycle are proposed to be a reduction of [**RuCO$_2$**]$^+$ to form [**RuCO$_2$**], followed by a C−O bond cleavage promoted by a proton and BIH$^+$, and finally, CO dissociation. The computational data show the reduction of [**RuCO$_2$**]$^+$ using BIH as a SED to be 20.4 kcal/mol uphill in energy (Figure 11, turnover-limiting step). However, considering [**RuBr**]^0 as the reducing agent this process is −16.5 kcal/mol downhill in energy. These energies indicate that following the generation of the active catalyst [**Ru**]$^+$, subsequent redox events between various species present in solution will likely become increasingly convoluted, and thus a determination of the true mechanism will be difficult without extensive spectral data.

Following the reduction of the CO$_2$ moiety to CO, the bond dissociation from [**RuCO**]$^+$ to [**Ru**]$^+$ is calculated to be 28.1 kcal/mol uphill in energy. Under light irradiation conditions, this process could be accelerated by visible light energy as photodissociation of carbonyl and other neutral ligands is common in the literature.[53,54] Presumably, the resting state in the cycle is the final TAS signal observed at 650 nm, and no intermediates beyond this are observed. The signal at ~530 nm appears to convert directly to the 650 nm signal, which suggests CO$_2$ associates with [**Ru**]$^+$ since this signal is not observed in the absence of CO$_2$. Incidentally, a similar shift from 528 to 678 nm

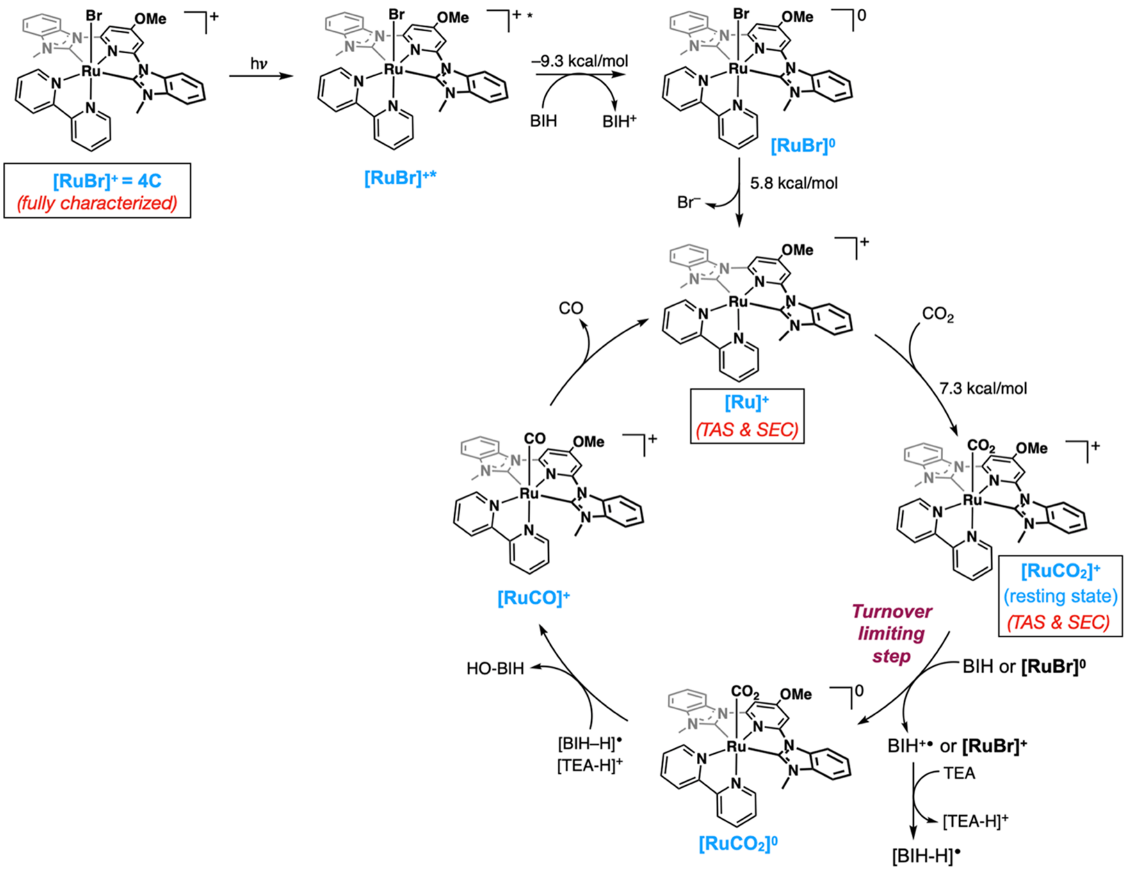

Figure 11. Proposed catalytic cycle based on DFT, TAS, and SEC studies. The boxed structures have experimental evidence (listed in red) to support their intermediacy in the catalytic cycle.

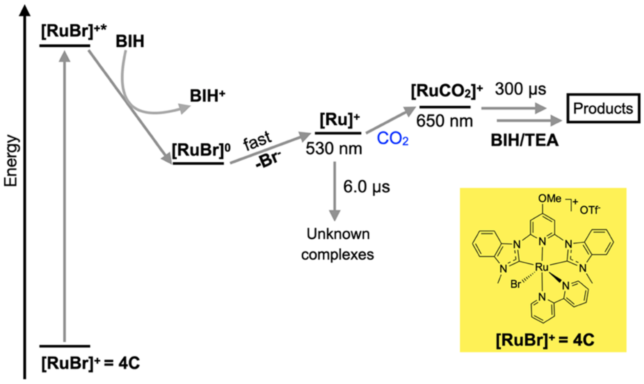

Figure 12. Timescales and energy landscape for each of the transformations of **4C** with BIH, TEA, and CO_2.

is found in the simulated UV spectra (see Figure 7 (bottom left) and Figures S45 and S46). If one of the steps following the formation of $[\mathbf{Ru}]^+$ is a reduction, the addition of a strong reductant to drive this intermediate forward in the catalytic cycle should result in increased TOF values. Indeed, addition of $Ir(ppy)_3$ to the system gives a stronger reductant than is anticipated from BIH (a weaker reductant but higher in concentration) or from $[\mathbf{RuBr}]^0$ (a stronger reductant than BIH). Thus, with $Ir(ppy)_3$, a significant increase in TOF (6.5 versus 395 h^{-1}) is observed, which is consistent with our proposed model and suggests reduction of the resting state occurs. Thus, reduction of $[\mathbf{RuCO_2}]^+$ appears to be the turnover-limiting step (Figure 11). Notably, no new signals would necessarily be expected from this added reductant if the remaining steps are relatively facile, and upon addition of $Ir(ppy)_3$ to the system, the signal at 650 nm is still observed as the dominant feature by TAS. Importantly, $[Ir(ppy)_3]^-$ is a stronger reductant than $[\mathbf{RuBr}]^0$, and reduction of **4C** to $[\mathbf{RuBr}]^0$ is highly favorable at −16.6 kcal/mol downhill in energy with $[Ir(ppy)_3]^-$.

Overall, these results suggest that the first four steps shown in Figure 12 are relatively rapid. Upon visible light irradiation under CO_2, the formation of $[\mathbf{RuCO_2}]^+$ occurs rapidly within the pulse duration (<10 ns) of the excitation laser. In contrast to rapid CO_2 binding, reduction of the $[\mathbf{RuCO_2}]^+$ resting state and subsequent C−O bond cleavage occurs more slowly. Collectively, these latter steps occur in about 330 μs, and these are the turnover-limiting steps in the catalytic cycle. The synthesis of improved catalysts will require optimizing the system to accelerate these later steps.

■ DISCUSSION AND CONCLUSIONS

In summary, we have described the synthesis and characterization of a series of ruthenium complexes supported by CNC pincers and bipyridine ligands for the photocatalytic reduction of CO_2 to CO. For $Ir(ppy)_3$-*sensitized* photocatalysis, benzimidazole-derived CNC ligands (**4A**−**4C**) were far more active than the imidazole-derived CNC pincer ligands (**2A**−**2B**) (Table 3). This is consistent with the reduction potentials shown in Table 2 and the reported reduction potential of $Ir(ppy)_3$ of −2.61 V,[55] which suggests that reduction of **2A** and **2B** will have a small driving force of only 150 mV based on their reduction potentials under Ar. In contrast, the more easily reduced benzimidazole-derived catalysts (**4A**−**4C**) will have a driving force of 260 mV for reduction by the reduced PS, $[Ir(ppy)_3]^-$, based on their reduction potentials under Ar (Table 2). We have observed a similar trend in our past work with more highly conjugated CNC pincers generally favoring faster TOF for photocatalytic CO_2 reduction.[21,34]

In contrast, for *self-sensitized* photocatalytic CO_2 reduction *without* $[Ir(ppy)_3]$, catalyst **4C** was the only catalyst to exhibit high activity ($TOF_{init} = 6.5\ h^{-1}$) from the earliest observed time points (Table 3 and Figures 5 and 6). The advantages of benzimidazole-derived NHC ligands have been mentioned above, but the reasons for enhancements with bromide (**4C**) vs chloride (**4A**) and CH_3CN (**4B**) monodentate ligands are unclear from the UV−vis and electrochemistry data (Table 2). Nonetheless, the advantages of **4C** have been well established for both sensitized and self-sensitized catalysis, and this catalyst was chosen for further studies. Self-sensitized catalysis is rare and eliminates the use of $Ir(ppy)_3$ as a precious metal PS and may have kinetic advantages for photoelectrochemical (PEC) applications. However, it is worth noting that $Ir(ppy)_3$-sensitized catalysis is inherently much faster, with larger TOF and TON values (Table 3).

The spectroelectrochemistry, transient absorption spectroscopy, and computational studies lead to our proposed mechanism for catalysis by **4C** and helps to explain some of the above-observed trends. Excitation of **4C** = $[\mathbf{RuBr}]^+$ generates $[\mathbf{RuBr}]^{+*}$, which leads to $[\mathbf{RuBr}]^0$ and is predicted to be downhill by −9.3 kcal/mol. The HOMO-LUMO plots (Figure S38) and NTO analysis (Figure S44) would suggest that $[\mathbf{RuBr}]^0$ is a Ru(II) complex with an anionic bpy ligand based upon the LUMO/LUTO being primarily bpy based. Bromide loss is then rapid and produces $[\mathbf{Ru}]^+$ at ∼530 nm under N_2 by TAS and SEC at 5.8 kcal/mol uphill. Under CO_2, this species is proposed to bind CO_2 leading to $[\mathbf{RuCO_2}]^+$ at 650 nm by TAS and SEC and 7.3 kcal/mol uphill. This species is the resting state under self-sensitized catalysis, but the consumption of this species speeds up in the presence of $Ir(ppy)_3$. Subsequent steps to complete the catalytic cycle from $[\mathbf{RuCO_2}]^+$ are proposed to involve electron transfer, C−O bond cleavage with concomitant O protonation, and CO loss to return to $[\mathbf{Ru}]^+$ in the catalytic cycle. Thus, the end result of this study is to suggest that further improvements in catalysis will need to target one of the above slow steps, with self-sensitized catalyst reduction being the most plausible slow step based on rapid formation of $[\mathbf{RuCO_2}]^+$ and a lack of further observed intermediates on the CO_2 reduction pathway.

■ EXPERIMENTAL SECTION

Synthetic Methods. The synthesis of all new compounds and spectral characterization is covered in the Supporting Information section.

Computational Methods. All computations were carried out using Revision C.01 of the Gaussian 16[56] suite of programs with default (10^{-8}) SCF convergence criteria. The PBE0 functional[57] in conjunction with Grimme's D3 empirical dispersion[58] and Becke-Johnson damping[59] [EMP = GD3BJ] was used for all computations. The basis set combination (BS1) is the Couty and Hall modification[60] (mod-LANL2DZ) to the valence basis set of LANL2DZ+ECP combination for Ru[61] and for C, H, N, and O the 6−31G(d′)[62−64] basis sets (the 6-31G(d′) basis sets have the d polarization functions taken from the 6-311G(d)[65] basis sets rather than the default value of 0.8[64] for C, N, and O). Spherical harmonic d functions were used throughout; *i.e.*, there are five angular basis functions per *d* function. The SMD solvation model was employed for all computations using parameters consistent with acetonitrile as the solvent.[66] Excited-state geometries were obtained from TD-DFT[67] optimizations using analytical gradients and solving the first five vertical excitations iteratively [TD(ROOT = 1,NSTATES = 5)] (TD-SMD-PBE0-D3BJ/BS1) or by variational DFT using a higher multiplicity reference wavefunction; the choice is noted by TD-DFT or DFT where appropriate. All stationary points were confirmed to be minima by an analytical frequency computation at the same level of theory. UV−vis absorption spectra were simulated using TD-DFT single points on the SMD-PBE0-D3BJ/BS1-optimized geometries (SMD-TD-DFT//SMD-PBE0-D3BJ/BS1). Emission spectra were simulated using TD-DFT single points on the optimized excited state-optimized geometries (SMD-TD-DFT//TD-SMD-PBE0-D3BJ/BS1). To simulate spectra of **2A**, **2B**, **4A**, **4B**, and **4C**, the first 30 vertical excitations from the optimized geometries were solved iteratively [TD(ROOT =1,NSTATES = 30)]. To simulate the spectra of various catalytic intermediates, the first 90 vertical excitations from the optimized geometries were solved iteratively [TD(ROOT = 1,NSTATES = 90)]. The simulated spectra were then generated using an in-house Fortran program by convoluting[68] the computed excitation energies and oscillator strengths with a Gaussian line-shape and a broadening of 20 or 35 nm. Orbital images were rendered in AGUI.

UV−vis Absorption Spectroscopy. Absorption spectra were recorded in a PerkinElmer Lambda 35 UV−vis Spectrometer using a cuvette of 1 cm pathlength under an ambient atmosphere. Five sample solutions with concentrations ranging from 20−60 μM for each complex in acetonitrile were used for the Beer's law plot. An aliquot of the sample solution was measured via UV−vis (200−700 nm). The absorbance at λ_{max} was plotted vs the concentration of the sample. The molar absorptivity was determined by calculating the slope of the line of best fit with the y-intercept = 0. Reported molar absorptivity values (ε) are listed in Table 2 in units of $M^{-1}\ cm^{-1}$.

Cyclic Voltammetry. Measurements were conducted using 1 mM analyte (Ru-complex) and 0.1 M supporting electrolyte (n-Bu_4PF_6) concentration in acetonitrile solvent with a sweep rate of 100 mV/s. The electrodes used are glassy carbon (working), platinum (counter), and $Ag/AgNO_3$ (reference). The Ar or CO_2 atmospheres were added by degassing through the solution. Before degassing, the solvent level was marked in the electrochemical chamber, and excess acetonitrile was added (∼3 mL). Then, the solution was degassed through an exit needle until the solvent level had returned to the original volume. Potentials are calibrated using ferrocene as a standard.

Transient Absorption Spectroscopy. Transient absorption spectroscopy measurements were performed using a commercial nanosecond laser flash photolysis spectrometer (LP980-KS, Edinburgh Instruments Ltd., Livingston, U.K.) at room temperature. Laser excitation at 355 nm (<10 mJ/pulse, 3−6 ns fwhm) was generated by a pulsed Nd:YAG laser (Continuum Surelite I, Amplitude) equipped with a doubling and tripling crystal, and the probe light was generated by a 150 W pulsed xenon arc lamp perpendicular to the pump source. Both single wavelength transient absorption and difference spectra were collected with a photomultiplier tube (PMT) detector (Hamamatsu R928) connected to a Tektronix model MDO3052 (200 MHz) digital oscilloscope. The probe background was collected between two laser shots and subtracted from the signal, and emission background was subtracted where relevant. A sealed 4 mm quartz cuvette was used for all TAS measurements, and the samples were purged with either N_2 or CO_2 for 10 min before the experiment began. For nsTAS measurements involving **4C** and $CoCp^*_2$ (with and without TEA), 1 kHz regeneratively amplified Ti:Sapphire laser (Coherent Astrella, Santa Clara, California) with a 7 W, sub-100 fs output pulse centered at 800 nm was split with an 85−15 beamsplitter to generate pump and probe beams. To generate the pump, the reflected portion of the 800 nm output was directed into a commercial optical parametric amplifier (OPerA Solo, Vilnius, Lithuania) to generate the 355 nm pump beam. Both the output of the OPerA Solo as well as the remainder of the originally transmitted 800 nm light were directed into a commercial transient absorption spectrometer (Ultrafast Systems Eos, Sarasota, Florida). The pump pulse was chopped at 500 Hz before being depolarized and focused with a 350 mm focal length lens to the sample position. An electronically delayed white fiber laser was used to generate the broadband continuum (350−900 nm). Pulses of the fiber laser were split into reference and probe beams before being passed onto the reference camera and onto the sample, respectively. nsTAS measurements were acquired by accumulating 100 data points over a 450 μs timescale during 8 min scans. The supplementary data was processed in the Igor Pro 8 software package.

ASSOCIATED CONTENT

Supporting Information

The Supporting Information is available free of charge at https://pubs.acs.org/doi/10.1021/acscatal.2c05459.

Experimental details on synthesis and characterization, single-crystal X-ray diffraction, cyclic voltammograms, time-resolved spectroscopy, photocatalysis, and computations (PDF)

Computational structures (XYZ)

Crystallographic information (CIF)

AUTHOR INFORMATION

Corresponding Authors

Nathan I. Hammer − *Department of Chemistry and Biochemistry, Coulter Hall, University of Mississippi, Oxford, Mississippi 38677, United States;* orcid.org/0000-0002-6221-2709; Email: nhammer@olemiss.edu

Jared H. Delcamp − *Department of Chemistry and Biochemistry, Coulter Hall, University of Mississippi, Oxford, Mississippi 38677, United States;* Present Address: Materials and Manufacturing Directorate, Air Force Research Laboratory, Wright-Patterson AFB, Ohio 45433, United States; UES, Inc., Dayton, Ohio 45432, United States; orcid.org/0000-0001-5313-4078; Email: delcamp@olemiss.edu, jared.delcamp.ctr@us.af.mil

Charles Edwin Webster − *Department of Chemistry, Mississippi State University, Starkville, Mississippi 39762, United States;* orcid.org/0000-0002-6917-2957; Email: ewebster@chemistry.msstate.edu

Elizabeth T. Papish − *Department of Chemistry and Biochemistry, University of Alabama, Tuscaloosa, Alabama 35487, United States;* orcid.org/0000-0002-7937-8019; Email: etpapish@ua.edu

Authors

Leigh Anna Hunt − *Department of Chemistry and Biochemistry, Coulter Hall, University of Mississippi, Oxford, Mississippi 38677, United States;* orcid.org/0000-0002-7681-3599

Sanjit Das − *Department of Chemistry and Biochemistry, University of Alabama, Tuscaloosa, Alabama 35487, United States;* orcid.org/0000-0003-4711-9933

Robert W. Lamb − *Department of Chemistry, Mississippi State University, Starkville, Mississippi 39762, United States;* orcid.org/0000-0001-6463-3809

Dinesh Nugegoda − *Department of Chemistry and Biochemistry, Coulter Hall, University of Mississippi, Oxford, Mississippi 38677, United States;* orcid.org/0000-0002-5456-8940

Christine Curiac − *Department of Chemistry and Biochemistry, Coulter Hall, University of Mississippi, Oxford, Mississippi 38677, United States;* orcid.org/0000-0003-2468-8906

Matthew T. Figgins − *Department of Chemistry, Mississippi State University, Starkville, Mississippi 39762, United States;* orcid.org/0000-0003-4391-3961

Ethan C. Lambert − *Department of Chemistry and Biochemistry, Coulter Hall, University of Mississippi, Oxford, Mississippi 38677, United States;* orcid.org/0000-0001-6893-9071

Fengrui Qu − *Department of Chemistry and Biochemistry, University of Alabama, Tuscaloosa, Alabama 35487, United States;* orcid.org/0000-0002-9975-2573

Complete contact information is available at: https://pubs.acs.org/10.1021/acscatal.2c05459

Author Contributions

[⊥]L.A.H., S.D. and R.W.L. contributed equally to this work.

Notes

The authors declare the following competing financial interest(s): E.T.P. and J.H.D. have filed a patent application related to this chemistry.

ACKNOWLEDGMENTS

The authors thank the NSF (CHE-1800281, 1800214, 1800201, 2102416, 2102511, and 2102552; OIA-1757220) for funding this research. The authors thank NSF CHE MRI 1828078 and UA for the purchase of the SC-XRD instrument. The authors thank NSF CHE MRI 1919906 and UA for the purchase of an NMR spectrometer. The authors thank Dr. Ken Belmore for assistance with the NMR experiments. The authors thank NSF MRI program (CHE 1726812, PI Cassady) and UA for the purchase of a MALDI TOF/TOF MS and Dr. Qiaoli Liang for MS experimental work. S.D. thanks the University of Alabama's Graduate Council Fellowship (GCF) for partial support. The computational work was completed with resources provided by the Mississippi State University High Performance Computing Collaboratory and the Mississippi Center for Supercomputing Research.

REFERENCES

(1) Elgrishi, N.; Chambers, M. B.; Wang, X.; Fontecave, M. Molecular polypyridine-based metal complexes as catalysts for the reduction of CO_2. *Chem. Soc. Rev.* **2017**, *46*, 761−796.

(2) Luo, Y.-H.; Dong, L.-Z.; Liu, J.; Li, S.-L.; Lan, Y.-Q. From molecular metal complex to metal-organic framework: The CO_2 reduction photocatalysts with clear and tunable structure. *Coord. Chem. Rev.* **2019**, *390*, 86−126.

(3) Morris, A. J.; Meyer, G. J.; Fujita, E. Molecular Approaches to the Photocatalytic Reduction of Carbon Dioxide for Solar Fuels. *Acc. Chem. Res.* **2009**, *42*, 1983−1994.

(4) Robert, M. Running the Clock: CO_2 Catalysis in the Age of Anthropocene. *ACS Energy Lett.* **2016**, *1*, 281−282.

(5) White, J. L.; Baruch, M. F.; Pander, J. E.; Hu, Y.; Fortmeyer, I. C.; Park, J. E.; Zhang, T.; Liao, K.; Gu, J.; Yan, Y.; Shaw, T. W.; Abelev, E.; Bocarsly, A. B. Light-Driven Heterogeneous Reduction of Carbon Dioxide: Photocatalysts and Photoelectrodes. *Chem. Rev.* **2015**, *115*, 12888−12935.

(6) Benson, E. E.; Kubiak, C. P.; Sathrum, A. J.; Smieja, J. M. Electrocatalytic and homogeneous approaches to conversion of CO_2 to liquid fuels. *Chem. Soc. Rev.* **2009**, *38*, 89−99.

(7) Leckel, D. Diesel Production from Fischer−Tropsch: The Past, the Present, and New Concepts. *Energy Fuels* **2009**, *23*, 2342−2358.

(8) Hawecker, J.; Lehn, J.-M.; Ziessel, R. Photochemical and Electrochemical Reduction of Carbon Dioxide to Carbon Monoxide Mediated by (2,2′-Bipyridine)tricarbonylchlororhenium(I) and Related Complexes as Homogeneous Catalysts. *Helv. Chim. Acta* **1986**, *69*, 1990−2012.

(9) Ishida, H.; Fujiki, K.; Ohba, T.; Ohkubo, K.; Tanaka, K.; Terada, T.; Tanaka, T. Ligand effects of ruthenium 2,2′-bipyridine and 1,10-phenanthroline complexes on the electrochemical reduction of CO_2. *J. Chem. Soc. Dalton Trans.* **1990**, *0*, 2155−2160.

(10) Behar, D.; Dhanasekaran, T.; Neta, P.; Hosten, C. M.; Ejeh, D.; Hambright, P.; Fujita, E. Cobalt Porphyrin Catalyzed Reduction of CO_2. Radiation Chemical, Photochemical, and Electrochemical Studies. *J. Phys. Chem. A* **1998**, *102*, 2870−2877.

(11) Tamaki, Y.; Morimoto, T.; Koike, K.; Ishitani, O. Photocatalytic CO_2 reduction with high turnover frequency and selectivity of formic acid formation using Ru(II) multinuclear complexes. *Proc. Natl. Acad. Sci. U.S.A.* **2012**, *109*, 15673−15678.

(12) Sato, S.; Morikawa, T.; Kajino, T.; Ishitani, O. A Highly Efficient Mononuclear Iridium Complex Photocatalyst for CO_2 Reduction under Visible Light. *Angew. Chem., Int. Ed.* **2013**, *52*, 988−992.

(13) Thoi, V. S.; Kornienko, N.; Margarit, C. G.; Yang, P.; Chang, C. J. Visible-Light Photoredox Catalysis: Selective Reduction of Carbon Dioxide to Carbon Monoxide by a Nickel N-Heterocyclic Carbene−Isoquinoline Complex. *J. Am. Chem. Soc.* **2013**, *135*, 14413−14424.

(14) Takeda, H.; Koizumi, H.; Okamoto, K.; Ishitani, O. Photocatalytic CO_2 reduction using a Mn complex as a catalyst. *Chem. Commun.* **2014**, *50*, 1491−1493.

(15) Nakada, A.; Koike, K.; Nakashima, T.; Morimoto, T.; Ishitani, O. Photocatalytic CO_2 Reduction to Formic Acid Using a Ru(II)−Re(I) Supramolecular Complex in an Aqueous Solution. *Inorg. Chem.* **2015**, *54*, 1800−1807.

(16) Sahara, G.; Ishitani, O. Efficient Photocatalysts for CO_2 Reduction. *Inorg. Chem.* **2015**, *54*, 5096−5104.

(17) Huckaba, A. J.; Sharpe, E. A.; Delcamp, J. H. Photocatalytic Reduction of CO_2 with Re-Pyridyl-NHCs. *Inorg. Chem.* **2016**, *55*, 682−690.

(18) Lee, S. K.; Kondo, M.; Okamura, M.; Enomoto, T.; Nakamura, G.; Masaoka, S. Function-Integrated Ru Catalyst for Photochemical CO_2 Reduction. *J. Am. Chem. Soc.* **2018**, *140*, 16899−16903.

(19) Shimoda, T.; Morishima, T.; Kodama, K.; Hirose, T.; Polyansky, D. E.; Manbeck, G. F.; Muckerman, J. T.; Fujita, E. Photocatalytic CO_2 Reduction by Trigonal-Bipyramidal Cobalt(II) Polypyridyl Complexes: The Nature of Cobalt(I) and Cobalt(0) Complexes upon Their Reactions with CO_2, CO, or Proton. *Inorg. Chem.* **2018**, *57*, 5486−5498.

(20) Shirley, H.; Su, X.; Sanjanwala, H.; Talukdar, K.; Jurss, J. W.; Delcamp, J. H. Durable Solar-Powered Systems with Ni-Catalysts for Conversion of CO_2 or CO to CH_4. *J. Am. Chem. Soc.* **2019**, *141*, 6617−6622.

(21) Das, S.; Rodrigues, R. R.; Lamb, R. W.; Qu, F.; Reinheimer, E.; Boudreaux, C. M.; Webster, C. E.; Delcamp, J. H.; Papish, E. T. Highly Active Ruthenium CNC Pincer Photocatalysts for Visible-Light-Driven Carbon Dioxide Reduction. *Inorg. Chem.* **2019**, *58*, 8012−8020.

(22) Benhamou, L.; Chardon, E.; Lavigne, G.; Bellemin-Laponnaz, S.; César, V. Synthetic Routes to N-Heterocyclic Carbene Precursors. *Chem. Rev.* **2011**, *111*, 2705−2733.

(23) Danopoulos, A. A.; Winston, S.; Motherwell, W. B. Stable N-functionalized ″pincer″ bis carbene ligands and their ruthenium complexes; synthesis and catalytic studies. *Chem. Commun.* **2002**, 1376−1377.

(24) Poyatos, M.; Mata, J. A.; Falomir, E.; Crabtree, R. H.; Peris, E. New Ruthenium(II) CNC-Pincer Bis(carbene) Complexes: Synthesis and Catalytic Activity. *Organometallics* **2003**, *22*, 1110−1114.

(25) Chianese, A. R.; Mo, A.; Lampland, N. L.; Swartz, R. L.; Bremer, P. T. Iridium Complexes of CCC-Pincer N-Heterocyclic Carbene Ligands: Synthesis and Catalytic C−H Functionalization. *Organometallics* **2010**, *29*, 3019−3026.

(26) Urgoitia, G.; SanMartin, R.; Herrero, M. T.; Domínguez, E. Palladium NCN and CNC pincer complexes as exceptionally active catalysts for aerobic oxidation in sustainable media. *Green Chem.* **2011**, *13*, 2161−2166.

(27) Yu, R. P.; Darmon, J. M.; Milsmann, C.; Margulieux, G. W.; Stieber, S. C. E.; DeBeer, S.; Chirik, P. J. Catalytic Hydrogenation Activity and Electronic Structure Determination of Bis(arylimidazol-2-ylidene)pyridine Cobalt Alkyl and Hydride Complexes. *J. Am. Chem. Soc.* **2013**, *135*, 13168−13184.

(28) Andrew, R. E.; Chaplin, A. B. Synthesis and Reactivity of NHC-Based Rhodium Macrocycles. *Inorg. Chem.* **2015**, *54*, 312−322.

(29) Huynh, H. V.; Han, Y.; Jothibasu, R.; Yang, J. A. ^{13}C NMR Spectroscopic Determination of Ligand Donor Strengths Using N-Heterocyclic Carbene Complexes of Palladium(II). *Organometallics* **2009**, *28*, 5395−5404.

(30) Scholl, M.; Ding, S.; Lee, C. W.; Grubbs, R. H. Synthesis and Activity of a New Generation of Ruthenium-Based Olefin Metathesis Catalysts Coordinated with 1,3-Dimesityl-4,5-dihydroimidazol-2-ylidene Ligands. *Org. Lett.* **1999**, *1*, 953−956.

(31) Helgert, T. R.; Hollis, T. K.; Oliver, A. G.; Valle, H. U.; Wu, Y.; Webster, C. E. Synthesis, Characterization, and X-ray Molecular Structure of Tantalum CCC-N-Heterocyclic Carbene (CCC-NHC) Pincer Complexes with Imidazole- and Triazole-Based Ligands. *Organometallics* **2014**, *33*, 952−958.

(32) Agarwal, J.; Shaw, T. W.; Stanton, C. J., III.; Majetich, G. F.; Bocarsly, A. B.; Schaefer, H. F., III. NHC-Containing Manganese(I) Electrocatalysts for the Two-Electron Reduction of CO_2. *Angew. Chem., Int. Ed.* **2014**, *53*, 5152−5155.

(33) Arikawa, Y.; Tabata, I.; Miura, Y.; Tajiri, H.; Seto, Y.; Horiuchi, S.; Sakuda, E.; Umakoshi, K. Photocatalytic CO_2 Reduction under Visible-Light Irradiation by Ruthenium CNC Pincer Complexes. *Chem. − Eur. J.* **2020**, *26*, 5603−5606.

(34) Das, S.; Nugegoda, D.; Yao, W.; Qu, F.; Figgins, M. T.; Lamb, R. W.; Webster, C. E.; Delcamp, J. H.; Papish, E. T. Sensitized and Self-Sensitized Photocatalytic Carbon Dioxide Reduction Under Visible Light with Ruthenium Catalysts Shows Enhancements with More Conjugated Pincer Ligands. *Eur. J. Inorg. Chem.* **2022**, *2022*, No. e202101016.

(35) Boudreaux, C. M.; Nugegoda, D.; Yao, W.; Le, N.; Frey, N. C.; Li, Q.; Qu, F.; Zeller, M.; Webster, E.; Delcamp, J. H.; Papish, E. T. Low Valent Cobalt(I) CNC Pincer Complexes as Catalysts for Light Driven Carbon Dioxide Reduction. *ACS Catal.* **2022**, *12*, 8718−8728.

(36) Papish, E. T.; Das, S.; Silprakob, W.; Boudreaux, C. M.; Manafe, S. Proton Responsive and Hydrogen Bonding Ligands in Organometallic Chemistry. In *Comprehensive Organometallic Chemistry IV*; Elsevier, 2021 DOI: 10.1016/B978-0-12-820206-7.00080-9.

(37) Shirley, H.; Figgins, M. T.; Boudreaux, C. M.; Liyanage, N. P.; Lamb, R. W.; Webster, C. E.; Papish, E. T.; Delcamp, J. H. Impact of the Dissolved Anion on the Electrocatalytic Reduction of CO_2 to CO with Ruthenium CNC Pincer Complexes. *ChemCatChem* **2020**, *12*, 4879−4885.

(38) Das, S.; Nugegoda, D.; Qu, F.; Boudreaux, C. M.; Burrow, P. E.; Figgins, M. T.; Lamb, R. W.; Webster, C. E.; Delcamp, J. H.; Papish, E. T. Structure Function Relationships in Ruthenium Carbon Dioxide Reduction Catalysts with CNC Pincers Containing Donor Groups. *Eur. J. Inorg. Chem.* **2020**, *2020*, 2709−2717.

(39) Boudreaux, C. M.; Liyanage, N. P.; Shirley, H.; Siek, S.; Gerlach, D. L.; Qu, F.; Delcamp, J. H.; Papish, E. T. Ruthenium(II) complexes of

pyridinol and N-heterocyclic carbene derived pincers as robust catalysts for selective carbon dioxide reduction. *Chem. Commun.* **2017**, *53*, 11217−11220.

(40) Burks, D. B.; Davis, S.; Lamb, R. W.; Liu, X.; Rodrigues, R. R.; Liyanage, N. P.; Sun, Y.; Webster, C. E.; Delcamp, J. H.; Papish, E. T. Nickel(II) pincer complexes demonstrate that the remote substituent controls catalytic carbon dioxide reduction. *Chem. Commun.* **2018**, *54*, 3819−3822.

(41) Chung, L.-H.; Cho, K.-S.; England, J.; Chan, S.-C.; Wieghardt, K.; Wong, C.-Y. Ruthenium(II) and Osmium(II) Complexes Bearing Bipyridine and the N-Heterocyclic Carbene-Based C^N^C Pincer Ligand: An Experimental and Density Functional Theory Study. *Inorg. Chem.* **2013**, *52*, 9885−9896.

(42) Arikawa, Y.; Nakamura, T.; Ogushi, S.; Eguchi, K.; Umakoshi, K. Fixation of atmospheric carbon dioxide by ruthenium complexes bearing an NHC-based pincer ligand: formation of a methylcarbonato complex and its methylation. *Dalton Trans.* **2015**, *44*, 5303−5305.

(43) Arikawa, Y.; Nakamura, T.; Higashi, T.; Horiuchi, S.; Sakuda, E.; Umakoshi, K. Reactivity of a Methoxido-Ruthenium Complex Bearing a Pincer-Type Bis(carbene) Ligand toward Thiocyanate, Carbon Disulfide, and Isothiocyanate. *Eur. J. Inorg. Chem.* **2017**, *2017*, 881−884.

(44) Reithmeier, R.; Bruckmeier, C.; Rieger, B. Conversion of CO_2 via Visible Light Promoted Homogeneous Redox Catalysis. *Catalysts* **2012**, *2*, 544.

(45) Genoni, A.; Chirdon, D. N.; Boniolo, M.; Sartorel, A.; Bernhard, S.; Bonchio, M. Tuning Iridium Photocatalysts and Light Irradiation for Enhanced CO_2 Reduction. *ACS Catal.* **2017**, *7*, 154−160.

(46) Rao, H.; Bonin, J.; Robert, M. Non-sensitized selective photochemical reduction of CO2 to CO under visible light with an iron molecular catalyst. *Chem. Commun.* **2017**, *53*, 2830−2833.

(47) Sato, S.; Morikawa, T. [Ir(tpy)(bpy)Cl] as a Photocatalyst for CO_2 Reduction under Visible-Light Irradiation. *ChemPhotoChem* **2018**, *2*, 207−212.

(48) Hawecker, J.; Lehn, J.-M.; Ziessel, R. Efficient photochemical reduction of CO_2 to CO by visible light irradiation of systems containing $Re(bipy)(CO)_3X$ or $[Ru(bipy)_3]^{2+}$-Co^{2+} combinations as homogeneous catalysts. *J. Chem. Soc., Chem. Commun.* **1983**, 536−538.

(49) Carpenter, C.; Brogdon, P.; McNamara, L.; Tschumper, G.; Hammer, N.; Delcamp, J. A Robust Pyridyl-NHC-Ligated Rhenium Photocatalyst for CO_2 Reduction in the Presence of Water and Oxygen. *Inorganics* **2018**, *6*, 22.

(50) Shirley, H.; Sexton, T. M.; Liyanage, N. P.; Palmer, C. Z.; McNamara, L. E.; Hammer, N. I.; Tschumper, G. S.; Delcamp, J. H. Effect of "X" Ligands on the Photocatalytic Reduction of CO_2 to CO with $Re(pyridylNHC\text{-}CF_3)(CO)_3X$ Complexes. *Eur. J. Inorg. Chem.* **2020**, *2020*, 1844−1851.

(51) Sun, Y.; Das, S.; Brown, S. R.; Blevin, E. R.; Qu, F.; Ward, N. A.; Gregory, S. A.; Boudreaux, C. M.; Kim, Y.; Papish, E. T. Ruthenium pincer complexes for light activated toxicity: Lipophilic groups enhance toxicity. *J. Inorg. Biochem.* **2023**, *240*, No. 112110.

(52) Coombe, V. T.; Heath, G. A.; MacKenzie, A. J.; Yellowlees, L. J. Spectroelectrochemical studies on tris(bipyridyl)iridium complexes: ultraviolet, visible and near-infrared spectra of the series $[Ir(bipyridyl)_3]^{3+/2+/+/0}$. *Inorg. Chem.* **1984**, *23*, 3423−3425.

(53) Tu, Y.-J.; Mazumder, S.; Endicott, J. F.; Turro, C.; Kodanko, J. J.; Schlegel, H. B. Selective Photodissociation of Acetonitrile Ligands in Ruthenium Polypyridyl Complexes Studied by Density Functional Theory. *Inorg. Chem.* **2015**, *54*, 8003−8011.

(54) Salassa, L.; Garino, C.; Salassa, G.; Gobetto, R.; Nervi, C. Mechanism of Ligand Photodissociation in Photoactivable $[Ru(bpy)_2L_2]^{2+}$ Complexes: A Density Functional Theory Study. *J. Am. Chem. Soc.* **2008**, *130*, 9590−9597.

(55) Rodrigues, R. R.; Boudreaux, C. M.; Papish, E. T.; Delcamp, J. H. Photocatalytic Reduction of CO_2 to CO and Formate: Do Reaction Conditions or Ruthenium Catalysts Control Product Selectivity? *ACS Appl. Energy Mater.* **2019**, *2*, 37−46.

(56) Frisch, M. J.; Trucks, G. W. S.; H, B.; Scuseria, G. E.; Robb, M. A.; Cheeseman, J. R.; Scalmani, G.; Barone, V.; Petersson, G. A.; Nakatsuji, H.; Li, X.; Caricato, M.; Marenich, A. V.; Bloino, J.; Janesko, B. G.; Gomperts, R.; Mennucci, B.; Hratchian, H. P.; Ortiz, J. V.; Izmaylov, A. F.; Sonnenberg, J. L.; Williams-Young, D.; Ding, F.; Lipparini, F.; Egidi, F.; Goings, J.; Peng, B.; Petrone, A.; Henderson, T.; Ranasinghe, D.; Zakrzewski, V. G.; Gao, J.; Rega, N.; Zheng, G.; Liang, W.; Hada, M.; Ehara, M.; Toyota, K.; Fukuda, R.; Hasegawa, J.; Ishida, M.; Nakajima, T.; Honda, Y.; Kitao, O.; Nakai, H.; Vreven, T.; Throssell, K.; Montgomery, J. A., Jr.; Peralta, J. E.; Ogliaro, F.; Bearpark, M. J.; Heyd, J. J.; Brothers, E. N.; Kudin, K. N.; Staroverov, V. N.; Keith, T. A.; Kobayashi, R.; Normand, J.; Raghavachari, K.; Rendell, A. P.; Burant, J. C.; Iyengar, S. S.; Tomasi, J.; Cossi, M.; Millam, J. M.; Klene, M.; Adamo, C.; Cammi, R.; Ochterski, J. W.; Martin, R. L.; Morokuma, K.; Farkas, O.; Foresman, J. B.; Fox, D. J. *Gaussian 16*; revision C.01; Gaussian, Inc.: Wallingford, CT, USA, 2016.

(57) Adamo, C.; Barone, V. Toward reliable density functional methods without adjustable parameters: The PBE0 model. *J. Chem. Phys.* **1999**, *110*, 6158−6170.

(58) Grimme, S. Semiempirical GGA-type density functional constructed with a long-range dispersion correction. *J. Comput. Chem.* **2006**, *27*, 1787−1799.

(59) Grimme, S.; Ehrlich, S.; Goerigk, L. Effect of the damping function in dispersion corrected density functional theory. *J. Comput. Chem.* **2011**, *32*, 1456−1465.

(60) Couty, M.; Hall, M. B. Basis sets for transition metals: Optimized outer p functions. *J. Comput. Chem.* **1996**, *17*, 1359−1370.

(61) Hay, P. J.; Wadt, W. R. Ab initio effective core potentials for molecular calculations. Potentials for K to Au including the outermost core orbitals. *J. Chem. Phys.* **1985**, *82*, 299−310.

(62) Hehre, W. J.; Ditchfield, R.; Pople, J. A. Self—Consistent Molecular Orbital Methods. XII. Further Extensions of Gaussian—Type Basis Sets for Use in Molecular Orbital Studies of Organic Molecules. *J. Chem. Phys.* **1972**, *56*, 2257−2261.

(63) Hariharan, P. C.; Pople, J. A. The influence of polarization functions on molecular orbital hydrogenation energies. *Theoret. Chim. Acta* **1973**, *28*, 213−222.

(64) Petersson, G. A.; Al-Laham, M. A. A complete basis set model chemistry. II. Open-shell systems and the total energies of the first-row atoms. *J. Chem. Phys.* **1991**, *94*, 6081−6090.

(65) McLean, A. D.; Chandler, G. S. Contracted Gaussian basis sets for molecular calculations. I. Second row atoms, Z = 11−18. *J. Chem. Phys.* **1980**, *72*, 5639−5648.

(66) Marenich, A. V.; Cramer, C. J.; Truhlar, D. G. Universal solvation model based on solute electron density and a continuum model of the solvent defined by the bulk dielectric constant and atomic surface tensions. *J. Phys. Chem. B* **2009**, *113*, 6378−6396.

(67) Marques, M. A. L.; Gross, E. K. U. Time-Dependent Density Functional Theory. *Annu. Rev. Phys. Chem.* **2004**, *55*, 427−455.

(68) Press, W. H. *Numerical Recipes in FORTRAN: the Art of Scientific Computing*, 2nd ed.; Cambridge University Press: Cambridge, England; New York, NY, USA, 1992; p 963.